ORIGINAL RESEARCH

Assessment of Gold-Coated Iron Oxide Nanoparticles as Negative T2 Contrast Agent in Small Animal MRI Studies

Stefania D Iancu[1,2]
Camelia Albu [1,3]
Liviu Chiriac [1,3,4]
Remus Moldovan[1,3]
Andrei Stefancu [1,2]
Vlad Moisoiu[1–3]
Vasile Coman[1,5]
Laszlo Szabo [1,2]
Nicolae Leopold [1,2]
Zoltán Bálint[1,2]

[1]IMOGEN Medical Research Institute, County Clinical Emergency Hospital, Cluj-Napoca 400012, Romania; [2]Faculty of Physics, Babeș-Bolyai University, Cluj-Napoca 400084, Romania; [3]Faculty of Medicine, Iuliu Hațieganu University of Medicine and Pharmacy, Cluj-Napoca 400349, Romania; [4]National Magnetic Resonance Center, Babeș-Bolyai University, Cluj-Napoca 400084, Romania; [5]Institute of Life Sciences, University of Agricultural Sciences and Veterinary Medicine Cluj-Napoca, Cluj-Napoca 400372, Romania

Purpose: Magnetic resonance imaging (MRI) contrast agents are pharmaceuticals that enable a better visualization of internal body structures. In this study, we present the synthesis, MRI signal enhancement capabilities, in vitro as well as in vivo cytotoxicity results of gold-coated iron oxide nanoparticles (Fe_3O_4@AuNPs) as potential contrast agents.

Methods: Fe_3O_4@AuNPs were obtained by synthesizing iron oxide nanoparticles and gradually coating them with gold. The obtained Fe_3O_4@AuNPs were characterized by spectroscopies, transmission electron microscopy (TEM) and energy dispersive X-ray diffraction. The effect of the nanoparticles on the MRI signal was tested using a 7T Bruker PharmaScan system. Cytotoxicity tests were made in vitro on Fe_3O_4@AuNP-treated retinal pigment epithelium cells by WST-1 tests and in vivo by following histopathological changes in rats after injection of Fe_3O_4@AuNPs.

Results: Stable Fe_3O_4@AuNPs were successfully prepared following a simple and fast protocol (<1h worktime) and identified using TEM. The cytotoxicity tests on cells have shown biocompatibility of Fe_3O_4@AuNPs at small concentrations of Fe ($<1.95\times10^{-8}$ mg/cell). Whereas, at higher Fe concentrations (eg 7.5×10^{-8} mg/cell), cell viability decreased to $80.88\pm5.03\%$, showing a mild cytotoxic effect. MRI tests on rats showed an optimal Fe_3O_4@AuNPs concentration of 6mg/100g body weight to obtain high-quality images. The histopathological studies revealed significant transient inflammatory responses in the time range from 2 hours to 14 days after injection and focal cellular alterations in several organs, with the lung being the most affected organ. These results were confirmed by hyperspectral microscopic imaging of the same, but unstained tissues. In most organs, the inflammatory responses and sublethal cellular damage appeared to be transitory, except for the kidneys, where the glomerular damage indicated progression towards glomerular sclerosis.

Conclusion: The obtained stable, gold covered, iron oxide nanoparticles with reduced cytotoxicity, gave a negative T_2 signal in the MRI, which makes them suitable for candidates as contrast agent in small animal MRI applications.

Keywords: MRI contrast agent, gold-coated iron oxide nanoparticles, cytotoxicity, D407 cells, histopathology, rats

Introduction

Magnetic resonance imaging (MRI) is a powerful imaging technique that uses magnetic fields to assess the morphological structure of organs in the body.[1] MRI uses contrast agents to obtain a better visualization of the body structures due to their enhanced contrast.[2] MRI contrast agents are a vibrant topic of research, especially since it has been shown that Gadolinium (Gd)-based contrast agents

Correspondence: Zoltán Bálint
Email zoltan.balint@phys.ubbcluj.ro

accumulate in the tissues for extended periods of time.[3,4] This is especially true for the brain,[5] which is an immunologically privileged site with a far less developed lymphatic system, features which prevent an efficient washout of the contrast agent. Although the clinical consequences of contrast agent accumulation are not clear, there is an ongoing quest to develop novel contrast agents with enhanced magnetic and biologic properties.[6] Moreover, there is a shift in paradigm towards combining the MRI contrast agent capabilities with other diagnostic or even therapeutic functions, leading to the so-called 'theranostic agents'.[7,8]

The first nanoparticle-based contrast agent approved by the FDA was represented by superparamagnetic iron oxide nanoparticles (SPION),[9,10] although they have been largely replaced by contrast agents based on Gd.[11] Both classes have an effect of reduction in T_1 relaxation times,[12] but the use of contrast agents with T_2 sequences is limited.[13]

Gold-coated iron oxide nanoparticles (Fe_3O_4@AuNPs) are a class of potential theranostic nanoparticles that have been studied for their multitude of magnetic and optical properties with possible medical applications.[14–18] Besides the MRI contrast agent capabilities conferred by the magnetic core, the collective oscillations of the electrons in the gold shell, also called plasmons, endow the Fe_3O_4@AuNPs with potential photothermal, photodynamic or surface-enhanced Raman scattering (SERS) capabilities.[19,20] Moreover, the gold-shell enables the easy functionalization of the Fe_3O_4@AuNPs with capping agents, antibodies or aptamers targeted at molecules that are differentially expressed in the tissue of interest.[21]

After the synthesis, by exploring the physical and biological properties, we sought to highlight the immense potential medical applications of Fe_3O_4@AuNPs. In this study, we present a wet chemistry protocol for synthesizing Fe_3O_4@AuNPs. We analyzed the characteristics of the obtained Fe_3O_4@AuNPs by various physico-chemical methods and tested the MRI signal enhancement capabilities of the Fe_3O_4@AuNPs by measuring the changes in T_2 relaxation time for different concentrations of nanoparticles suspended in physiological serum. Moreover, the MRI performance of Fe_3O_4@AuNPs was tested in vivo by comparing images of rats injected with NPs with saline-injected controls. The cytotoxicity of Fe_3O_4@AuNPs was tested in vitro on D407 cells and in vivo in rats up to 2 weeks post-injection. The accumulation of Fe_3O_4@AuNPs in the different organs and their inflammation was assessed by histopathological analyses.

These analyses were complemented by hyperspectral microscopy data from the same organs.

Materials and Methods
Synthesis of Fe_3O_4@AuNPs

Fe_3O_4 nanoparticles (Fe_3O_4NPs) were synthesized by adapting the protocol reported by Kang et al.[22] Thus, 0.85 mL of 12 N HCl was added to 25 mL of ultrapure H_2O (Millipore, resistivity >18 MΩ). Then, 5.2 g of $FeCl_3$ and 2 g of $FeCl_2$ were dissolved in the HCl solution and mixed with 250 mL of 1.5 M NaOH. The black precipitate consisting of Fe_3O_4NPs was washed four times using a strong magnet and then resuspended in 250 mL of ultrapure H_2O with 1 mL of 1.5 M NaOH added. To stabilize the Fe_3O_4NPs, the colloid was mixed with an equal volume of 0.1 M glucose.

To cover the Fe_3O_4NPs with a gold shell, 20 mL of as-synthesized Fe_3O_4NPs stabilized with glucose were added to 40 mL of H_2O, heated to 85°C and then mixed with 2 mL of 1% $HAuCl_4$. The resulting colloid was kept at 85°C for 20 min to ensure the complete reduction of Au. Then, the colloid was washed using a strong magnet to eliminate the unbounded AuNPs and resuspended in 60 mL of ultrapure H_2O. The washing procedure was performed three times. Finally, the colloid was stabilized by adding 500 μL of 0.1 M glucose.

To improve the thickness and the uniformity of the Au shell, the covering steps were repeated twice. Before the second covering step, 1 mL of 1% NaOH was added to the Fe_3O_4@AuNPs to increase the pH of the solution, along with 30 mL of 0.1 M glucose (step mandatory for the reduction of Au). All reagents were purchased from Sigma-Aldrich.

Characterization of Fe_3O_4@AuNPs
Inductively Coupled Plasma Optical Emission Spectroscopy (ICP-OES)

The amounts of Fe and Au in Fe_3O_4NPs and Fe_3O_4@AuNPs were quantified using ICP-OES performed on a Perkin-Elmer-OPTIMA 2100 DV device. For this, the NPs were sonicated and then atomized with aqua regia. The detection of Fe was based on the 238.204 nm line (limit of detection 0.01 mg/L), while Au was measured based on the 267.595 nm line (limit of detection 0.02 mg/L). To assess the influence of the Au shell on the interaction between the NPs and cells, we also measured the amount of Fe and Au in human retinal pigment epithelium cells (D407 cells) incubated with

NPs for 24 h. After incubation, the cells were detached from cell culture plate using trypsin, counted, atomized with aqua regia and analyzed by ICP-OES.

Physical and Chemical Characterization

The NPs were characterized in terms of size, stability and morphology. UV-Vis spectra were acquired using a Jasco V-630 spectrometer, with a spectral resolution of 2 nm. The transmission electron microscopy (TEM) images and energy-dispersive X-ray diffraction (EDX) measurements were acquired using a JEOL, JEM-100CX electron microscope operated at 200 kV. For this, 10 μL of Fe_3O_4 @AuNPs was deposited onto a Cu grid and dried at room temperature. Zeta potential measurements were performed using a ZetaSizer ZS (Malvern) on liquid samples.

Ethical Statement and Regulatory Compliance

The studies were conducted in accordance with Good Laboratory Practice standards. The welfare and treatment of the animals were maintained in accordance with the general principles governing the use of animals in experiments as defined by the European Communities (Directives 86/609/ EEC, 2010/63/EU). The study protocol was reviewed and approved by the Ethics Committee of the "Iuliu Haţieganu" University of Medicine and Pharmacy Cluj-Napoca, Romania and by the Ethics Committee of the Sanitary and Veterinary Directorate for Food Safety, Cluj-Napoca, Romania.

MRI Experiments

All samples were analyzed using a 7 Tesla Bruker PharmaScan 50/16 USP (Bruker BioSpin MRI GmbH, Ettlingen, Germany) dual resonance system.

The relaxometry quantitative analyzes were performed in vitro, using the RARE T_1+T_2-map protocol, which allows the calculation of relaxation times T_1 and T_2.[23] The mechanism by which these protocols calculate the two relaxation times is based on the variation of the repetition time (TR), the echo time (TE) between the RF $\pi/2$ and π. A single section was recorded with 5 TE variations and 6 times variations. The Fe_3O_4@AuNPs were diluted in psychological serum at different concentrations (1:1, 1:6, 1:10 and 1:50). All samples were measured using identical conditions.

MRI acquisitions on animal models (Wistar rats) were performed with the TurboRARE-T_2 protocol, dedicated to imaging for T_2 relaxation time. Fe_3O_4@AuNPs at concentrations between 2 and 10 mg/100 g body weight were injected in the left ventricle to ensure a fast spread to all

organs (typically 3–5 s). The image protocol consisted of a 2D MultiTri-pilot geometry with a 5–6 cm field of view, slice thickness of 0.8 mm, interslice thickness 1.3 mm, and 3x5 images in axial, sagittal, and coronal positions. Repetition time was set to 80 ms, echo time was 11 ms, matrix of 256x256 pixels, with 0.181–0.225 cm/pixel. The number of scans was set to 1 for all Tri-pilot type scans.

We estimated the signal-to-noise ratio (SNR) and contrast-to-noise ratio (CNR) from the MR images of rats treated with Fe_3O_4@AuNPs using methods and classical definitions described in the literature.[24,25] Briefly, SNR was calculated for renal cortex by dividing the average signal intensity of two regions of interest (ROIs) one from the renal cortex and one from the air outside the imaged object. CNR represented the contrast between renal cortex and paravertebral muscle. Mean signal intensity from ROI delimited in paravertebral muscle was subtracted from mean signal intensity from ROI delimited in renal cortex and the result was divided by noise (ROI in air outside the imaged object).

In vitro Cytotoxicity of Fe_3O_4@AuNPs

The cytotoxicity of the Fe_3O_4@AuNPs was assessed using WST-1 tests, which were performed on 96-well plates using D407 cells (This retinal pigment epithelium cell line was kindly donated by Prof. em. Dr. Dr.h.c. Horst A. Diehl from University of Bremen). For this, $8x10^3$ D407 cells per well were grown on Dulbecco's modified Eagle's medium, enriched with L-glutamine, fetal bovine serum and 1% penicillin/streptomycin. The cells were grown at 37°C, 5% CO_2, and 45% relative humidity for 24h. The cells were then incubated for 24h with different concentrations of Fe_3O_4@AuNPs (0.00008–0.004 mg/mL Fe). Before treatment, the NPs were centrifuged and resuspended in cellular medium. Cells treated with the same amount of cell medium and grown in the same conditions were used as control group. For the WST-1 tests, formazan was solubilized with dimethyl sulfoxide for 1h before measuring the absorbance at 630 nm and 570 nm (background) using an Epoch Microplate Spectrophotometer (Biotek Instruments). The measurements were performed in triplicate. The statistical analysis used to determine the in vitro toxicity of the NPs consisted of one-way ANOVA followed by Dunnett´s test and it was performed using GraphPad Prism Version 6.01 (GraphPad Software). The test compares the mean of each group with the one from the control group, no matching or pairing being attributed between groups. The significance level was set to 0.05

(95% confidence interval). The results of cytotoxicity of the Fe_3O_4@AuNPs were normalized to the control group.

In vivo Cytotoxicity of Fe_3O_4@AuNPs
Study Design

A total of 35 male Wistar rats (body weight 150–180 g) were assigned to 7 groups: group 0 used as controls, and groups 1–6, based on the NPs exposure duration (2 h, 6 h, 24 h, 72 h, 7 days and 14 days). All animals were kept in identical conditions throughout the study. Groups 1–6 received an injection of 0.1 mL Fe_3O_4@AuNPs saline solution at a concentration of 6 mg/100 g body weight, while the controls received 0.1 mL physiological serum. After the pre-established exposure times, the animals were euthanized with 0.2 mL Ketamine per 100 g body weight after pre-anesthesia with 0.1 mL Ketamine per 100 g body weight. Tissue samples from heart, lungs, liver, spleen, kidney, brain, skeletal muscle, thigh bone and sternum from all 35 rats were collected. Samples from each organ were taken for histopathological processing and microscopic examination.

Bone fragments were immersed in Osteodec solution prior to sectioning and processing. Paraffin-embedded tissues were sectioned and stained before microscopic examination. In order to better evaluate pathological changes and lesions, the following staining methods were used for each case: Hematoxylin-Eosin, Masson's Trichrome and Silver stain according to the standard protocols. Specific immunostaining was used for further analysis, when needed (eg, vimentin, CD34). The microscopic slides were than examined by the pathologist, using an Olympus BX46 clinical microscope (Olympus Europe SE & Co, Hamburg, Germany) with an LED illuminator, configured with a 2x plan apochromatic objective and microscopic changes were noted. Inflammatory response and degenerative changes were noted as mild, moderate and severe. All observed lesions were registered and used for further statistical analyses.

For image acquisition, representative slides were scanned using 3D HISTECH 1.22 SPI Pannoramic scanner (3dhistech ltd, Budapest, Hungary) with 20x Plan-Apochromat objective. The acquired images were examined using the 3D HISTECH software Case Viewer 2.2.

We used a CytoViva Imaging System 2.5 (CytoViva, Inc.; Auburn, AL, USA) for hyperspectral imaging. The dark-field microscope included an Olympus BX43 microscope. We used an UPL Fluorite 60x Iris oil immersion objective to acquire the images. For illumination, we employed a halogen lamp and a CytoViva Optical Illuminator. In short, light is generated by a halogen lamp and then partly blocked by an aperture and focused by a condenser toward the sample (ie the tissue section). The incoming light interacts with the sample and non-scattered light is blocked by an additional aperture. Only the scattered light reaches the objective lens. The light is detected by either an optical charge-coupled device (CCD) camera or a hyperspectral camera. The gained information is combined into a single image of the tissue.

Results and Discussion
Synthesis and Characterization of Fe_3O_4@AuNPs

We synthesized Fe_3O_4@AuNPs by starting with Fe_3O_4 NPs cores, onto which we sequentially added layers of Au shell in a two-step procedure. The presented protocol represents an original method of synthesizing Au-covered magnetic NPs using only simple wet chemistry. The whole synthesis process could be accomplished in less than 1 h.

Covering the Fe_3O_4NPs with gold shell by gold reduction onto the surface of the nanoparticles mediated by citrate or glucose was reported before.[14,15,26-29] However, the presented procedures used large amount of gold or were time-consuming.[14,27,28] The gold shell is formed either by using a glue material between gold and Fe_3O_4 NPs like silica with NH_2,[27] or by using a long synthesis method that requires argon medium.[28] The novelty of our protocol is represented by a fast synthesis method that uses glucose for binding the gold to the Fe_3O_4NPs surface and for reducing gold from its salt. By using glucose as a reduction agent for gold, the price for Fe_3O_4NPs fabrication can be lowered compared to coating methods that use oleylamine,[30] oleic acid or poly-L-histidine.[31]

In our study, the synthesis steps used for Fe_3O_4@Au are adapted from the method described by Carneiro et al,[17] where citrate is used as a reducing agent for gold, as in the synthesis of gold NPs.[32] The citrate replaces the OH^- groups from Fe_3O_4NPs surface and reduces the gold from its salt right on the surface of NPs. Moreover, Fe_3O_4@AuNPs reduced by citrate can be functionalized with other molecules.[26,31,33] In our study, citrate was replaced by glucose, which is also used for NP functionalization.

The reduction of Au^{3+} from its salt by using an organic reducing agent is the easiest way of forming a gold shell onto Fe_3O_4. Sodium citrate, oleylamine or sodium borohydride were often used in order to reduce gold and form citrate capped gold NPs.[29,31] However, in most studies, the

reducing agent was added in the mixture of gold and Fe_3O_4NPs, gold was reduced by citrate, and AuNPs affixed to Fe_3O_4. In our study, the reducing agent is on top of the Fe_3O_4, acting like a glue for gold on top of the Fe_3O_4NPs.

Additionally, glucose was chosen owing to the sodium-glucose transporters present in the cell membrane that facilitate the cellular uptake of glucose.[34] It was previously shown that glucose-coated Fe_3O_4NPs and AuNPs were internalized in a higher concentration than NPs coated with other surfactants.[35,36] Moreover, previous literature results showed a reduced biocompatibility of Fe_3O_4 @AuNPs produced with some reducing agents (eg hydroxylamine).[37]
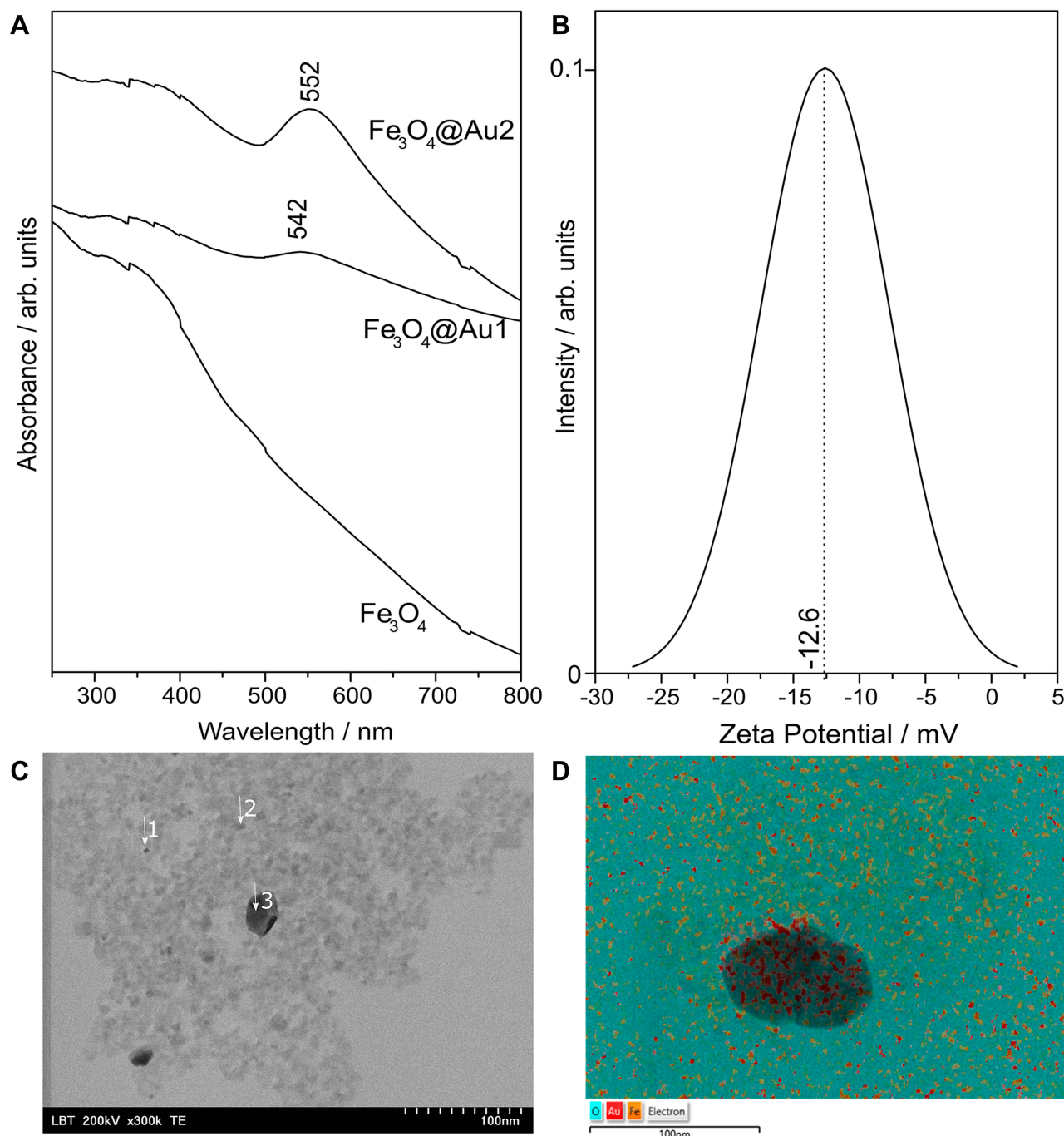
Figure 1 (**A**) UV-Vis absorption spectra of Fe_3O_4NPs and Fe_3O_4@AuNPs after the first (Fe_3O_4@Au1) and second (Fe_3O_4@Au2) covering steps; (**B**) zeta potential of the final Fe_3O_4@AuNPs; (**C**) typical TEM image of Fe_3O_4@AuNPs; and (**D**) the corresponding elemental composition of O, Fe and Au measured via EDX.

The UV-Vis spectrum of Fe_3O_4NPs depicted a characteristic broad peak centered at 342 nm attributed to Fe_3O_4 (Figure 1A). The figure also shows the UV-Vis spectrum of $Fe_3O_4@AuNPs$ after the first and second deposition of Au. Compared to the UV-Vis spectrum of Fe_3O_4NPs, the spectrum of $Fe_3O_4@AuNPs$ presents a peak around 540 nm, determined by the surface plasmon resonance of the Au shell. It has been reported that glucose-stabilized gold nanoparticles exhibit a strong surface plasmonic peak at 540 nm, for nanoparticles with diameter of 19 nm.[38] In the case of the $Fe_3O_4@AuNPs$ covered with layers of Au in two steps, the surface plasmon resonance peak is shifted towards higher wavelengths, indicating that the thickness of the Au shell has increased. Moreover, the surface plasmon resonance peak is both sharper and more intense in the case of $Fe_3O_4@AuNPs$ covered with Au in two steps, suggesting that the Au shell became more uniform in the latter case. Performing a third covering step did not lead to a further improvement, as indicated by the UV-Vis absorption, suggesting that two repeats were enough to completely cover the Fe_3O_4 core with Au shell (Supplementary Figure S1). Thus, subsequent tests were performed solely for $Fe_3O_4@AuNPs$ covered two times with Au.

The Au shell on Fe_3O_4NPs includes the NPs in the group of theranostic agents, expanding their applicability domain from MR imaging to the photothermal field also. Tódor et al[39] showed that AuNPs Localized Surface Plasmon Resonance (LSPR) at around 530–540 nm convert efficiently the light coming from a 532 nm laser into heat. However, with increasing NP size, the LSPR peak is shifted to the red region of the spectrum and the photothermal domain of NPs is also shifted to higher wavelengths. $Fe_3O_4@AuNPs$ with an absorbance peak at 580 nm coming from the gold shell have been previously used for photothermal therapy with cells exposed 1–5 min to near-infrared irradiation.[14] LSPR peak of the gold shell at lower wavelengths (552 nm) leads to a blue shift of the domain of the photothermal capability of $Fe_3O_4@AuNPs$, as it was shown for simple AuNPs.

For in vivo use, in order to improve their biocompatibility and cellular uptake, functionalization of Fe_3O_4 @AuNPs with different organic molecules (eg ascorbic acid, citrate) were reported.[40,41] Thus, in our experiments, after the second step of gold deposition on Fe_3O_4NPs, a small quantity of glucose was added not only to stabilize the NPs, but also to improve the internalization of Fe_3O_4 @AuNPs in cells.

Table 1 The Fe and Au Content of Fe_3O_4NPs and Fe_3O_4 @AuNPs as Measured by Inductively Coupled Plasma Optical Emission Spectroscopy (ICP-OES)

	Fe (µg/mL)	Au (µg/mL)
Fe_3O_4NPs	5.436	–
$Fe_3O_4@AuNPs$	0.405	2.01

Table 2 The Results of the Elemental Analysis of Fe_3O_4 @AuNPs for Points Depicted in Figure 2, Calculated Using EDX (Values are mean±SD)

Points	%Fe	%O	%Au
1	38.4±1.9	16.5±3.0	45.1±2.3
2	40.8±1.8	16.9±2.8	42.3±2.1
3	1.0±0.2	11.0±0.6	88.0±0.6

The concentrations of Fe and Au in the $Fe_3O_4@AuNPs$ and Fe_3O_4NPs colloidal solutions were measured using ICP-OES (Table 1), showing that after two deposition steps gold is attached to Fe_3O_4NPs. Of note, we obtained a Fe concentration of $Fe_3O_4@AuNPs$ around 13 times lower than that of the initial Fe_3O_4NPs because of the several washing steps performed during the synthesis process.

To assess the stability of the $Fe_3O_4@AuNPs$, we performed Zeta potential measurements several days after synthesis. The example results depicted in Figure 1B show
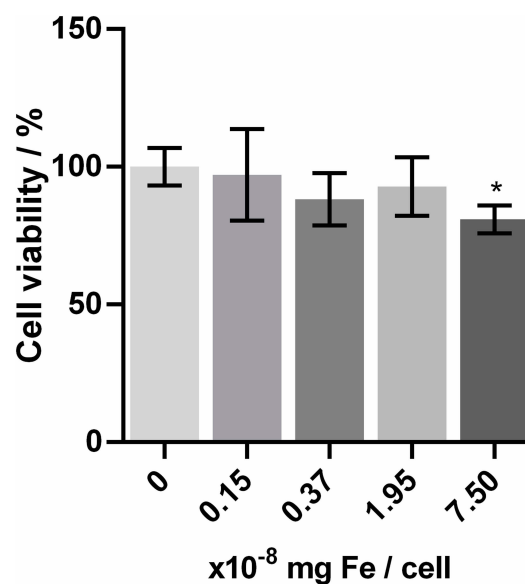

Figure 2 The results of the D407 cell viability (WST-1 test) for different concentrations of $Fe_3O_4@AuNPs$.
Notes: Data are presented as mean ± SD. The $Fe_3O_4@AuNP$ concentration used for cells treatment is presented in Supplementary Table S1. *Statistically significant difference as compared to control ($p<0.05$).

that the Zeta potential of the Fe_3O_4@Au NPs nanoparticles reaches a mean value of –12.6 mV. Compared to NPs with a positive zeta potential, negatively charged NPs are repelled by the negative charge of cellular membranes, leading to better cytotoxicity profiles.[42]

Next, we characterized the Fe_3O_4@AuNPs using transmission electron microscopy (TEM – typical images are presented in Figure 1C) and energy dispersive X-ray diffraction (EDX). The results of the TEM measurements showed small (2–3 nm) NPs, which aggregated during the drying process of the sample preparation for TEM. The results of the EDX elemental analysis for the points depicted in Figure 1D showed that Fe and Au are present simultaneously in the same spots (Table 2), thus demonstrating the successful synthesis of core/shell Fe_3O_4@AuNPs.

Cytotoxicity and Cellular Internalization

To test the cytotoxicity of the NPs, we performed WST-1 tests on D407 cells. The gold shell of Fe_3O_4@AuNPs improves the biocompatibility of the nanoparticles,[27] but their cytotoxicity increases at high concentration. The limit of biocompatibility of Fe_3O_4@AuNPs is spread on a wide range depending on their morphological properties, reducing agent and surfactant. For example, Feridex (an FDA approved SPIO contrast agent) was reported to be biocompatible for a concentration up to 50 µg/mL Fe. However, not all of these NPs were internalized, since the iron concentration was just 6.53±0.34 pg Fe/cell.[43] The

reduced cellular uptake of Fe_3O_4NPs was also demonstrated by other researchers, where NPs were coated with different organic molecules such as dextran,[44] polyethylene glycol (PEG) or polyethyleneimine (PEI).[45] The cell internalization rate can be increased by covering the Fe_3O_4 NPs with gold.

Thus, the molecules used to cover the Fe_3O_4@AuNPs influence their cytotoxicity, too.[46] For example, some studies reported cytotoxicity at already 0.05 mg/mL Fe_3O_4 @AuNPs concentration.[47] However, covering them with organic molecules led to increased biocompatibility up to 0.1–0.4 mg/mL Fe_3O_4@AuNPs,[27,47] or even a tolerance till 2 mg/mL was observed, when they were coated with doxorubicin.[48] It was shown that covering them with PEG led to an improvement of their cellular uptake,[49] but it also increased the diameter of nanoparticles. Glucose can play the same role as a covering agent, but without big differences in the resulting nanoparticle's diameter. The results of the WST-1 test for Fe_3O_4@AuNPs on the D407 cells are presented in Figure 2. The Dunnett's test showed that, except for the highest concentration, none of the others had a significant difference in viability compared to the control group (numerical results presented in Supplementary Table 1), suggesting that Fe_3O_4NPs exhibit low toxicity on D407 cells up till the 7.5×10^{-8} mg Fe/cell concentration (0.004 mg/mL Fe). The effective Fe concentrations for the solutions used for treating the cells are presented in Supplementary Table 2, together with the Fe concentrations in a single cell. The Fe concentration per
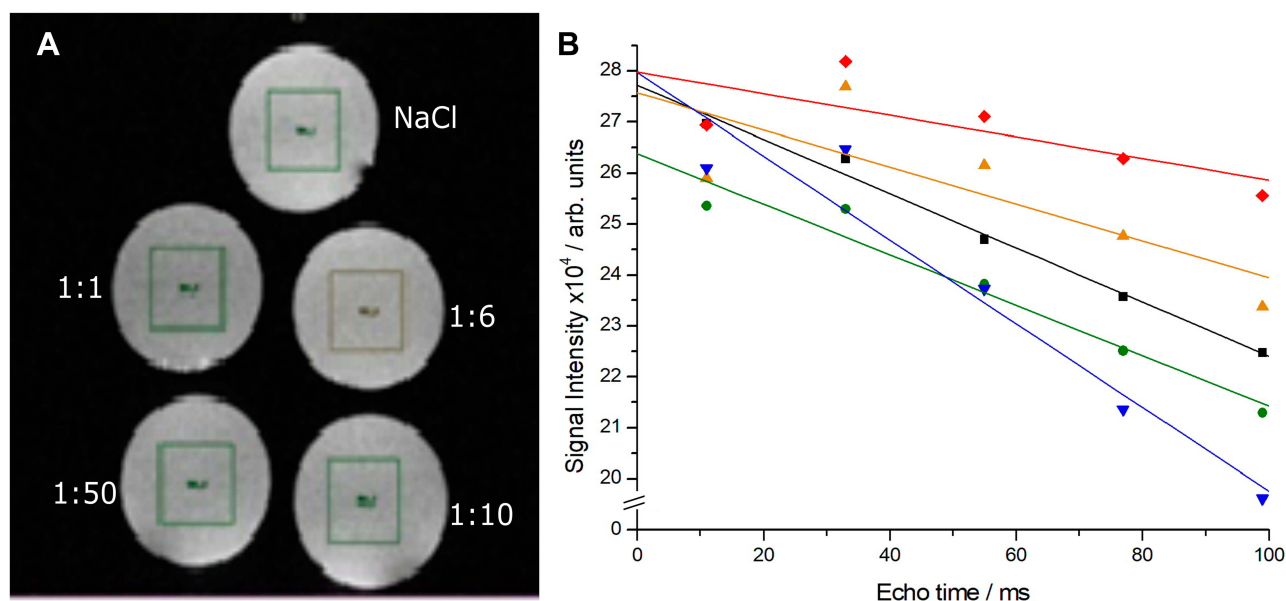

Figure 3 (**A**) MR images of the vials and (**B**) relaxometry curves for 4 dilutions of Fe_3O_4@AuNPs (1:50, 1:10, 1:6, 1:1) and for the NaCl control.
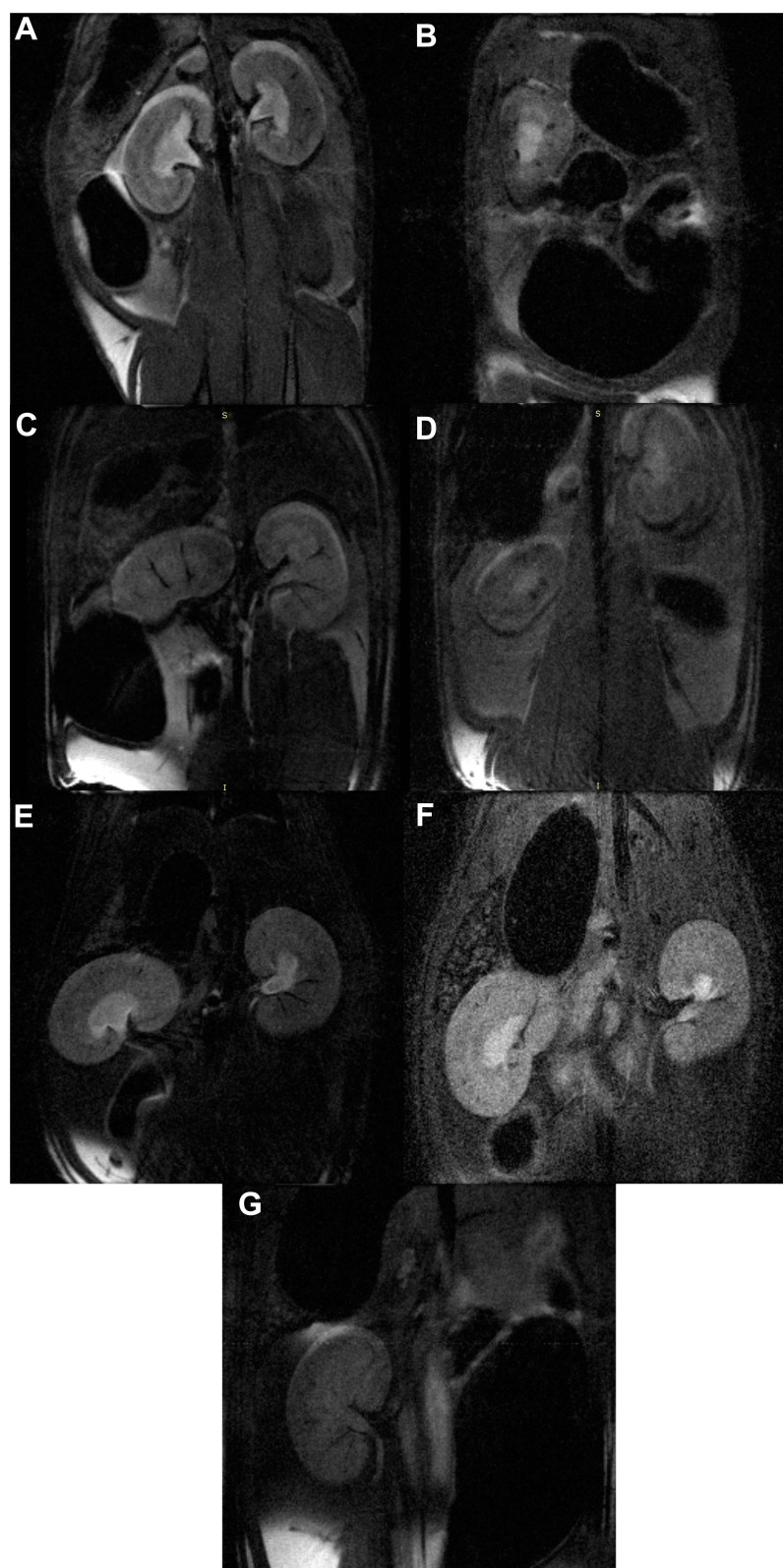
Figure 4 In vivo MR images of contrast evolution of Fe$_3$O$_4$@Au NPs in rats (**A**) saline control, at (**B**) 0 h, (**C**) 2 h, (**D**) 6 h, (**E**) 24 h, (**F**) 7 days, and (**G**) 14 days post-injection.

Table 3 Signal-to-Noise Ratio (SNR) and Contrast-to-Noise Ratio (CNR) of the MR Images of Rats Treated with Fe_3O_4@AuNPs at Different Time Intervals Post-Injection (Up to 14 Days)

Time Since Injection	SNR	CNR
Control	5.52	0.45
0 h	6.91	2.60
2 h	7.20	4.66
6 h	3.90	1.54
24 h	5.70	3.39
7 d	5.12	1.85
14 d	3.71	1.40

Notes: The signal intensity was measured on the slices presented in Figure 4A–G. The collecting points for each MR image are detailed in Supplementary Figure S2 (A-K).

cell was calculated by dividing the Fe concentration of the colloidal solutions used to treat the cells (determined by ICP-OES measurements) by the number of cells treated.

MRI Tests

The relaxometry curves of the NP solutions (Figure 3A) showed a decrease in intensity with the addition of Fe_3O_4@AuNPs, proving a dose-dependent effect on the signal (Figure 3B). The in vivo MRI tests showed a clear difference between the animals injected with Fe_3O_4@AuNPs and controls (Figure 4). Moreover, a dose of 6 mg/100 g body weight proved to be the optimal choice for obtaining good quality images.

The estimated values of SNR and CNR are presented in Table 3. The MR image analysis from the moment of injection (Figure 4A) and up to 2 weeks post-injection (Figure 4B–G and Table 3) showed that the contrast in the animal model increases to a maximum at 2 h post-injection (SNR: 5.52 for the control and 7.2 for the 2h, and CNR: 0.45 for the control and 4.66 for the 2h,

respectively), and then decreases gradually, suggesting that the majority of the Fe_3O_4@AuNPs are either removed from the tissue or assimilated after 1 week post-injection. The values were determined from the regions of interest presented in Supplementary Figure S2 (A-K).

Histopathology in Rats

Histopathological examination revealed mostly transient inflammatory responses (Figure 5A) and focal cellular alterations in several organs in our study (Figure 5B). In longer studies, even after one year of the treatment, excretion of nanoparticles was found in liver and spleen of mice treated with gold covered Fe_3O_4NPs.[50] In our study, moderate changes were observed in heart and spleen. The same response regarding the accumulation of nanoparticles in spleen was reported for PEG-coated or polymer-coated Fe_3O_4@AuNPs.[50] For our animals, no significant changes were observed in brain and sternum (bone/cartilage) (Figure 6).

The most affected organ was the lung with persistent inflammatory response even after 14 days post-injection. The lung presented severe inflammatory infiltrate in the alveolar septae. On a panoramic view, the inflammatory response can be easily seen. While in groups 1–3 (2 h, 6 h, 24 h after exposure to NPs) the inflammation was mainly focal, in groups 4 and 5 (72 h and 7 days after exposure to NPs, respectively) we could observe a diffuse involvement of the lung surface. Even though in group 6 (14 days after exposure to NPs) the inflammatory response is reduced, the thickening of the alveolar walls remains, therefore we used immunostaining for Vimentin to assess fibroblastic proliferation. A statistical analysis showed that the inflammatory infiltrate in the lung reaches a peak at 24–72 h after injection, and then decreases in intensity, but remains at an elevated level (Supplementary Figure S3). Relevant in vivo studies showed
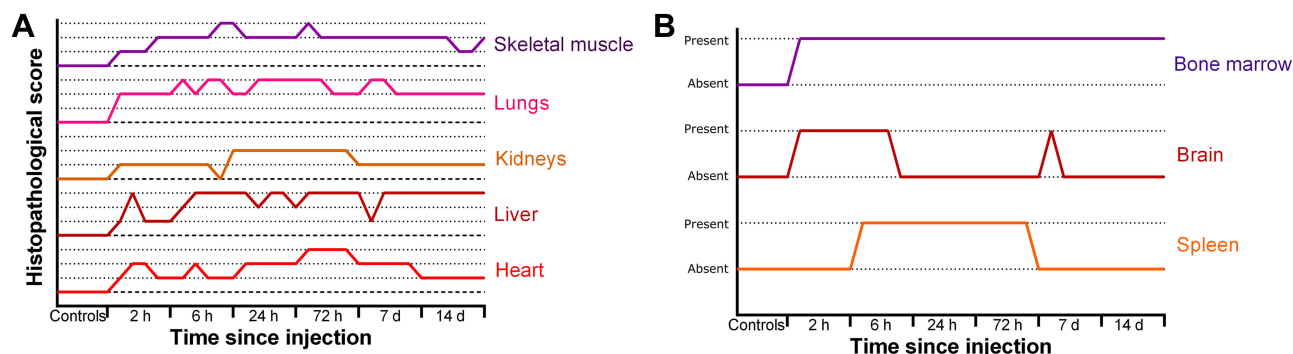

Figure 5 Overall evaluation of inflammatory response (**A**) and cellular damage (**B**) after injection of Fe_3O_4@AuNPs in rats.

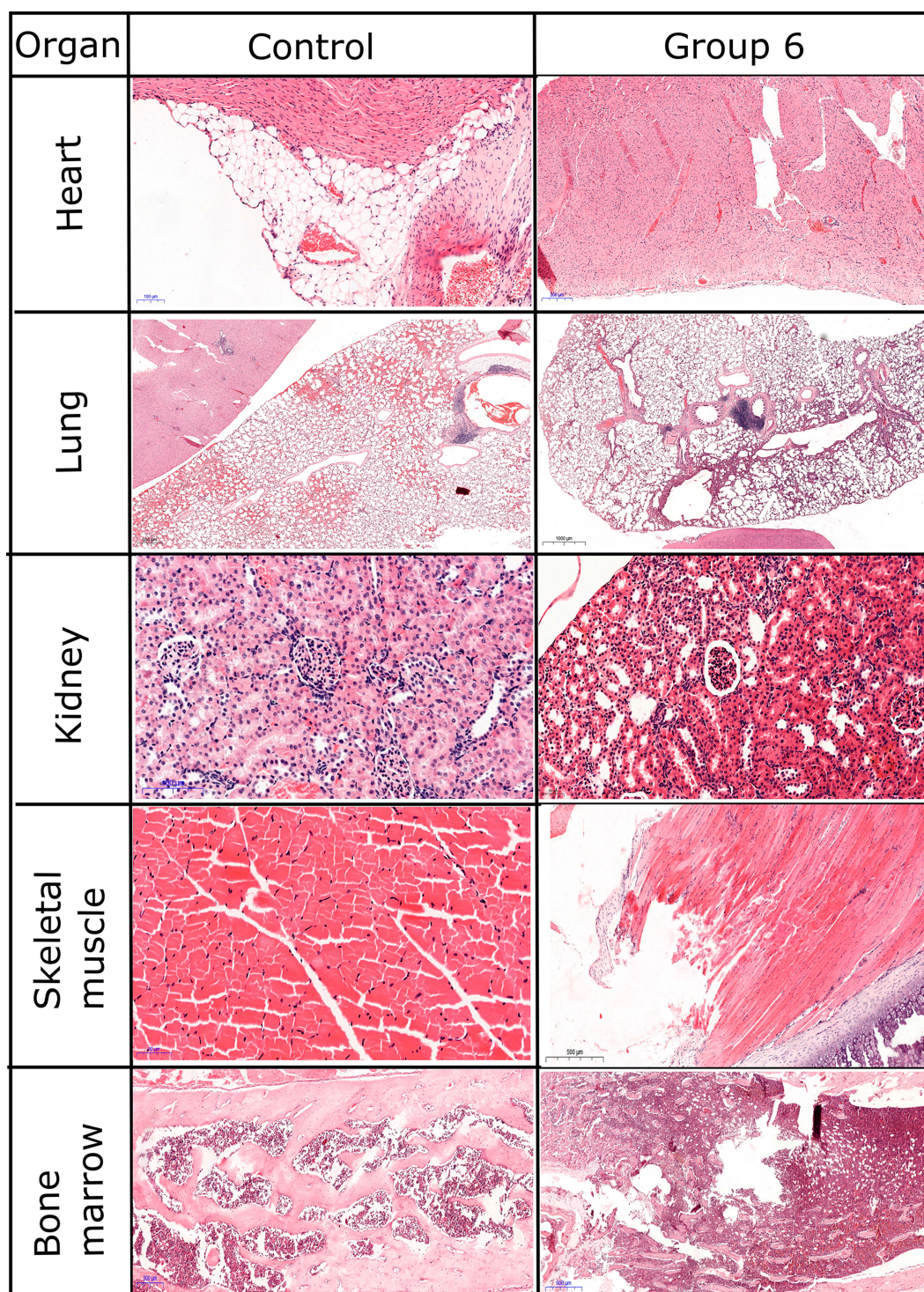| Organ	Control	Group 6
Heart		
Lung		
Kidney		
Skeletal muscle		
Bone marrow		

Figure 6 Histopathological evaluation of inflammatory response.

that Fe_3O_4NPs induce the secretion of pro-inflammatory cytokines, leading to chronic dysfunction of lungs.[51] If the gold shell is dissolved in spleen, residuals of Fe_3O_4NPs could be re-circulated through the body. Liver examination revealed moderate inflammatory infiltrate in the portal space. Small foci of intralobular inflammation were observed, as well. The inflammation could be a result of the dissolution of nanoparticles in tissues, as Kolosnjaj-Tabi et al demonstrated that after 90 days the gold shell thickness decreased to half of the initial one.[50] In our samples, moderate degenerative lesions were observed. In group 6, vacuolar degeneration was also observed in pericentrolobular hepatocytes. Complementary
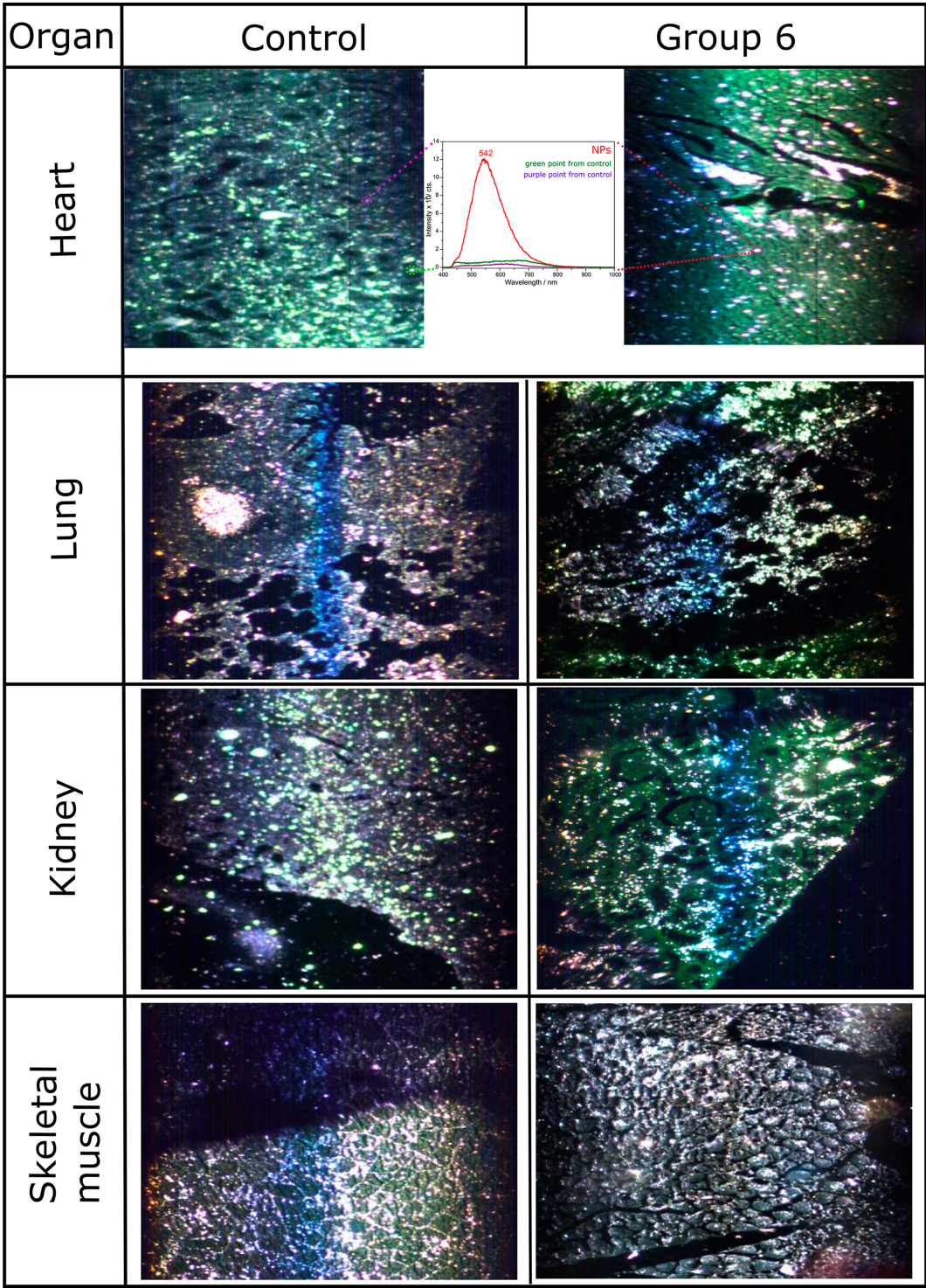
Figure 7 Hyperspectral images of inflammatory response on the same, but unstained samples as used for Figure 6.
Note: Inset shows the corresponding spectra of the marked points (red for NP-treated, green and purple - control).

staining did not reveal any sign of fibrosis or fibroblastic changes in examined slides.

In kidneys, mild inflammatory response and mild focal tubular necrosis were observed at 2 h after nanoparticle injection (group 1). Inflammatory response was localized in the interstitium, with a peak at 24–72 h (Figure 6). However, its intensity decreased at 2 weeks post-injection, thus showing a transient signal. Still, mild tubular necrosis was present

even after 2 weeks (Supplementary Figure S4). Glomerular hypercellularity was observed starting 24 h after injection and was visible in the kidneys obtained from rats sacrificed at 14 days post-injection. Immunostaining for CD34, a marker for endothelial cells, revealed a decrease in number of glomerular capillaries and increase in mesangial cellularity (Supplementary Figure S5). In group 6, vimentin staining showed a diffuse and homogenous staining, thus suggesting a possible progression to glomerular fibrosis.

Both cardiac and skeletal muscle presented severe, but transient inflammatory responses, and focal cellular damage. The inflammatory response in the cardiac muscle was decreased in intensity at 14 days post-injection (Supplementary Figure S6), while in skeletal muscle it was long-lasting (Figures 5 and 6). Similarly, other studies reported an excretion of nanoparticles from the whole body (eg heart, kidney, spleen, brain, lungs), except for liver, after 14 days post-injection.

A similar response was observed in the hematopoietic tissues also. In the spleen, follicular hyperplasia was the main change, and it regressed at 14 days after injection. Bone marrow showed immediate hypercellularity with increased megakaryocytes that persisted in all examined specimens. Brain tissue examination showed isolated neuronal cell death and focal gliosis, but the changes were inconstant and sparse in our study group. Sternum fragments examination did not exhibit any histological changes.

Hyperspectral imaging of tissue biopsies holds great potential for rapid and quantitative analysis since it can be used without staining and relies only on the intrinsic absorbance/scattering of light from the cellular components. Although exhaustive studies on hyperspectral imaging of tissue biopsies are still scarce, it was shown that hyperspectral imaging allows detection and quantification of cellular changes such as malignancy or inflammatory response. Moreover, hyperspectral imagining is suitable for nanoparticle detection in solution (eg silver nanoparticles, titanium dioxide nanoparticles), in vitro in cells treated with nanoparticles or even ex vivo in unstained tissues from mice injected with nanoparticles.[52,53]

The scattering cross-section of metallic nanoparticles is proportional to ~R^6, yielding thus a high scattering rate, making them easily detectable through dark field microscopy which detects only the scattered light. Figure 7 shows the potential of hyperspectral imaging to capture morphological changes at the tissue level without staining. Indeed, in the heart sections of the treated animals, the Fe_3O_4@AuNPs could be easily identified based on their surface plasmon resonance (marked by the red squares). These hyperspectral images confirm the above observations of NP accumulation in the regions. However, besides the identification of Fe_3O_4@AuNPs in the heart tissue sections, no other tissue had specific signal. It has been reported earlier that Fe_3O_4NPs coated with dextran or PEG accumulate in organs like spleen, kidneys, and liver with an excretion time longer than one month.[54] The in vivo effects of our NPs showed a decrease in inflammation after 3–7 days for spleen and kidneys, probably due to the protective gold shell.

Conclusion

We present a simple and fast protocol for gold-coated iron oxide nanoparticle synthesis. The obtained stable nanoparticles gave a negative T2 signal in vivo in MRI experiments after injection in rats. Their reduced cytotoxicity in vitro and mainly transient inflammation in vivo qualifies these nanoparticles as possible candidates for contrast agent in small animal MRI applications.

Acknowledgments

Funding

Disclosure

Stefania D Iancu, Laszlo Szabo, Nicolae Leopold and Zoltán Bálint report a patent Method of Nanoparticle Synthesis with Magnetic Core and Gold Shell pending to A/00571/16.09.2019 - OSIM, Romania. Vlad Moisoiu reports a patent Synthesis method for glucose-stabilized gold

magnetoplasmonic nanoparticles pending. The authors declare no other conflicts of interest.

References

1. Shokrollahi H. Contrast agents for MRI. *Mater Sci Eng C*. 2013;33 (8):4485–4497. doi:10.1016/j.msec.2013.07.012

2. Sun C, Lee JSH, Zhang M. Magnetic nanoparticles in MR imaging and drug delivery. *Adv Drug Del Rev*. 2008;60(11):1252–1265. doi:10.1016/j.addr.2008.03.018

3. Kanda T, Fukusato T, Matsuda M, et al. Gadolinium-based contrast agent accumulates in the brain even in subjects without severe renal dysfunction: evaluation of autopsy brain specimens with inductively coupled plasma mass spectroscopy. *Radiology*. 2015;276(1):228–232. doi:10.1148/radiol.2015142690

4. McDonald RJ, McDonald JS, Kallmes DF, et al. Intracranial gadolinium deposition after contrast-enhanced MR imaging. *Radiology*. 2015;275(3):772–782. doi:10.1148/radiol.15150025

5. Boyken J, Frenzel T, Lohrke J, Jost G, Pietsch H. Gadolinium accumulation in the deep cerebellar nuclei and globus pallidus after exposure to linear but not macrocyclic gadolinium-based contrast agents in a retrospective pig study with high similarity to clinical conditions. *Invest Radiol*. 2018;53(5):278–285. doi:10.1097/RLI.0000000000000440

6. Wahsner J, Gale EM, Rodríguez-Rodríguez A, Caravan P. Chemistry of MRI contrast agents: current challenges and new frontiers. *Chem Rev*. 2019;119(2):957–1057. doi:10.1021/acs.chemrev.8b00363

7. Ho SL, Cha H, Oh IT, et al. Magnetic resonance imaging, gadolinium neutron capture therapy, and tumor cell detection using ultrasmall Gd2O3 nanoparticles coated with polyacrylic acid-rhodamine B as a multifunctional tumor theragnostic agent. *RSC Adv*. 2018;8 (23):12653–12665. doi:10.1039/C8RA00553B

8. Prabhu P, Patravale V. The upcoming field of theranostic nanomedicine: an overview. *J Biomed Nanotechnol*. 2012;8(6):859–882. doi:10.1166/jbn.2012.1459

9. Qiao R, Yang C, Gao M. Superparamagnetic iron oxide nanoparticles: from preparations to in vivo MRI applications. *J Mater Chem*. 2009;19(35):6274–6293. doi:10.1039/b902394a

10. Laurent S, Forge D, Port M, et al. Magnetic iron oxide nanoparticles: synthesis, stabilization, vectorization, physicochemical characterizations and biological applications. *Chem Rev*. 2008;108(6):2064–2110. doi:10.1021/cr068445e

11. Runge VM. Critical questions regarding gadolinium deposition in the brain and body after injections of the gadolinium-based contrast agents, safety, and clinical recommendations in consideration of the EMA's pharmacovigilance and risk assessment committee recommendation for suspension of the marketing authorizations for 4 linear agents. *Invest Radiol*. 2017;52(6):317–323. doi:10.1097/RLI.0000000000000374

12. De Leõn-rodríguez LM, Martins AF, Pinho MC, Rofsky NM, Sherry AD. Basic MR relaxation mechanisms and contrast agent design. *J Magn Reson Imaging*. 2015;42(3):545–565. doi:10.1002/jmri.24787

13. Xiao S, Yu X, Zhang L, et al. Synthesis of peg-coated, ultrasmall, manganese-doped iron oxide nanoparticles with high relaxivity for t1/ t2 dual-contrast magnetic resonance imaging. *Int J Nanomedicine*. 2019;14:8499–8507. doi:10.2147/IJN.S219749

14. Nassireslami E, Ajdarzade M. Gold coated superparamagnetic iron oxide nanoparticles as effective nanoparticles to eradicate breast cancer cells via photothermal therapy. *Adv Pharm Bull*. 2018;8 (2):201–209. doi:10.15171/apb.2018.024

15. Ahmad T, Bae H, Rhee I, Chang Y, Jin SU, Hong S. Gold-coated iron oxide nanoparticles as a T 2 agent in magnetic resonance imaging. *J Nanosci Nanotechnol*. 2012;12(7):5132–5137. doi:10.1166/jnn.2012.6368

16. Neshastehriz A, Khosravi Z, Ghaznavi H, Shakeri-Zadeh A. Gold-coated iron oxide nanoparticles trigger apoptosis in the process of thermo-radiotherapy of U87-MG human glioma cells. *Radiat Environ Biophys*. 2018;57(4):405–418. doi:10.1007/s00411-018-0754-5

17. Carneiro MFH, Machado ART, Antunes LMG, et al. Gold-coated superparamagnetic iron oxide nanoparticles attenuate collagen-induced arthritis after magnetic targeting. *Biol Trace Elem Res*. 2019. doi:10.1007/s12011-019-01799-z

18. Peng XH, Qian X, Mao H, et al. Targeted magnetic iron oxide nanoparticles for tumor imaging and therapy. *Int J Nanomedicine*. 2008;3(3):311–321. doi:10.2147/ijn.s2824

19. Lee DK, Song Y, Tran VT, Kim J, Park EY, Lee J. Preparation of concave magnetoplasmonic core-shell supraparticles of gold-coated iron oxide via ion-reducible layer-by-layer method for surface enhanced Raman scattering. *J Colloid Interface Sci*. 2017;499:54–61. doi:10.1016/j.jcis.2017.03.098

20. Jain PK, Xiao Y, Walsworth R, Cohen AE. Surface plasmon resonance enhanced magneto-optics (SuPREMO): faraday rotation enhancement in gold-coated iron oxide nanocrystals. *Nano Lett*. 2009;9(4):1644–1650. doi:10.1021/nl900007k

21. Daniel MC, Astruc D. Gold nanoparticles: assembly, supramolecular chemistry, quantum-size-related properties, and applications toward biology, catalysis, and nanotechnology. *Chem Rev*. 2004;104 (1):293–346. doi:10.1021/cr030698+

22. Kang YS, Risbud S, Rabolt JF, Stroeve P. Synthesis and characterization of nanometer-size Fe3O4 and γ-Fe2O3 particles. *Chem Mater*. 1996;8(9):2209–2211. doi:10.1021/cm960157j

23. Hoehn-berlar M, Eis M, Back T, Kohno K, Yamashita K. Changes of relaxation times (T1, T2) and apparent diffusion coefficient after permanent middle cerebral artery occlusion in the rat: temporal evolution, regional extent, and comparison with histology. *Magn Reson Med*. 1995;34(6):824–834. doi:10.1002/mrm.1910340607

24. Kaufman L, Kramer DM, Crooks LE, Ortendahl DA. Measuring signal-to-noise ratios in MR imaging. *Radiology*. 1989;173 (1):265–267. doi:10.1148/radiology.173.1.2781018

25. Welvaert M, Rosseel Y. On the definition of signal-to-noise ratio and contrast-to-noise ratio for fMRI data. *PLoS One*. 2013;8(11). doi:10.1371/journal.pone.0077089

26. Lo CK, Xiao D, Choi MMF. Homocysteine-protected gold-coated magnetic nanoparticles: synthesis and characterisation. *J Mater Chem*. 2007;17(23):2418–2427. doi:10.1039/b617500g

27. Keshtkar M, Shahbazi-Gahrouei D, Mehrgardi MA, Aghaei M, Khoshfetrat SM. Synthesis and cytotoxicity assessment of gold-coated magnetic iron oxide nanoparticles. *J Biomed Phys Eng*. 2018;8(4):357–364.

28. Pal S, Morales M, Mukherjee P, Srikanth H. Synthesis and magnetic properties of gold coated iron oxide nanoparticles. *J Appl Phys*. 2009;105(7):07B504. doi:10.1063/1.3059607

29. Moraes Silva S, Tavallaie R, Sandiford L, Tilley RD, Gooding JJ. Gold coated magnetic nanoparticles: from preparation to surface modification for analytical and biomedical applications. *Chem Commun*. 2016;52(48):7528–7540. doi:10.1039/C6CC03225G

30. Smith M, McKeague M, DeRosa MC. Synthesis, transfer, and characterization of core-shell gold-coated magnetic nanoparticles. *MethodsX*. 2019;6:333–354. doi:10.1016/j.mex.2019.02.006

31. Jin Y, Jia C, Huang SW, O'Donnell M, Gao X. Multifunctional nanoparticles as coupled contrast agents. *Nat Commun*. 2010;1(4). doi:10.1038/ncomms1042

32. Brown KR, Walter DG, Natan MJ. Seeding of colloidal Au nanoparticle solutions. 2. Improved control of particle size and shape. *Chem Mater*. 2000;12(2):306–313. doi:10.1021/cm980065p

33. Ghorbani M, Hamishehkar H, Arsalani N, Entezami AA. Preparation of thermo and pH-responsive polymer@Au/Fe3O4 core/shell nanoparticles as a carrier for delivery of anticancer agent. *J Nanopart Res*. 2015;17(7). doi:10.1007/s11051-015-3097-z

34. Navale AM, Paranjape AN. Glucose transporters: physiological and pathological roles. *Biophys Rev.* 2016;8(1):5–9. doi:10.1007/s12551-015-0186-2

35. Barbaro D, Di Bari L, Gandin V, et al. Glucose-coated superparamagnetic iron oxide nanoparticles prepared by metal vapour synthesis are electively internalized in a pancreatic adenocarcinoma cell line expressing GLUT1 transporter. *PLoS One.* 2015;10(4):e0123159. doi:10.1371/journal.pone.0123159

36. Gromnicova R, Davies HA, Sreekanthreddy P, et al. Glucose-coated gold nanoparticles transfer across human brain endothelium and enter astrocytes in vitro. *PLoS One.* 2013;8(12):e81043. doi:10.1371/journal.pone.0081043

37. Guo Y, Zhang Z, Kim DH, et al. Photothermal ablation of pancreatic cancer cells with hybrid iron-oxide core gold-shell nanoparticles. *Int J Nanomedicine.* 2013;8:3437–3446. doi:10.2147/IJN.S47585

38. Suvarna S, Das U, Kc S, et al. Synthesis of a novel glucose capped gold nanoparticle as a better theranostic candidate. *PLoS One.* 2017;12(6):e0178202. doi:10.1371/journal.pone.0178202

39. Tódor IS, Szabó L, Marişca OT, Chiş V, Leopold N. Gold nanoparticle assemblies of controllable size obtained by hydroxylamine reduction at room temperature. *J Nanopart Res.* 2014;16(12). doi:10.1007/s11051-014-2740-4

40. Sood A, Arora V, Shah J, Kotnala RK, Jain TK. Multifunctional gold coated iron oxide core-shell nanoparticles stabilized using thiolated sodium alginate for biomedical applications. *Mater Sci Eng C.* 2017;80:274–281. doi:10.1016/j.msec.2017.05.079

41. Zhao X, Cai Y, Wang T, Shi Y, Jiang G. Preparation of alkanethiolate-functionalized core/shell Fe3O4@Au nanoparticles and its interaction with several typical target molecules. *Anal Chem.* 2008;80(23):9091–9096. doi:10.1021/ac801581m

42. Frohlich E. The role of surface charge in cellular uptake and cytotoxicity of medical nanoparticles. *Int J Nanomedicine.* 2012;7:5577–5591. doi:10.2147/IJN.S36111

43. Bu L, Xie J, Chen K, et al. Assessment and comparison of magnetic nanoparticles as MRI contrast agents in a rodent model of human hepatocellular carcinoma. *Contrast Media Mol Imaging.* 2012;7(4):363–372. doi:10.1002/cmmi.494

44. Unterweger H, Janko C, Schwarz M, et al. Non-immunogenic dextran-coated superparamagnetic iron oxide nanoparticles: a biocompatible, size-tunable contrast agent for magnetic resonance imaging. *Int J Nanomedicine.* 2017;12:5223–5238. doi:10.2147/IJN.S138108

45. Feng Q, Liu Y, Huang J, Chen K, Huang J, Xiao K. Uptake, distribution, clearance, and toxicity of iron oxide nanoparticles with different sizes and coatings. *Sci Rep.* 2018;8(1):1–3. doi:10.1038/s41598-018-19628-z

46. Pisanic TR 2nd, Blackwell JD, Shubayev VI, Finones RR, Jin S. Nanotoxicity of iron oxide nanoparticle internalization in growing neurons. *Biomaterials.* 2007;28(16):2572–2581. doi:10.1016/j.biomaterials.2007.01.043

47. Mohammad F, Balaji G, Weber A, Uppu RM, Kumar CSSR. Influence of gold nanoshell on hyperthermia of super paramagnetic iron oxide nanoparticles (SPIONs). *J Phys Chem C Nanomater Interfaces.* 2010;114(45):19194–19201. doi:10.1021/jp105807r

48. Gupta AK, Gupta M. Cytotoxicity suppression and cellular uptake enhancement of surface modified magnetic nanoparticles. *Biomaterials.* 2005;26(13):1565–1573. doi:10.1016/j.biomaterials.2004.05.022

49. Lartigue L, Hugounenq P, Alloyeau D, et al. Cooperative organization in iron oxide multi-core nanoparticles potentiates their efficiency as heating mediators and MRI contrast agents. *ACS Nano.* 2012;6(12):10935–10949. doi:10.1021/nn304477s

50. Kolosnjaj-Tabi J, Javed Y, Lartigue L, et al. The one year fate of iron oxide coated gold nanoparticles in mice. *ACS Nano.* 2015;9(8):7925–7939. doi:10.1021/acsnano.5b00042

51. Kornberg TG, Stueckle TA, Antonini JA, et al. Potential toxicity and underlying mechanisms associated with pulmonary exposure to iron oxide nanoparticles: conflicting literature and unclear risk. *Nanomaterials (Basel, Switzerland).* 2017;7(10). doi:10.3390/nano7120458

52. Roth GA, Tahiliani S, Neu-Baker NM, Brenner SA. Hyperspectral microscopy as an analytical tool for nanomaterials. *Wiley Interdiscip Rev Nanomed Nanobiotechnol.* 2015;7(4):565–579. doi:10.1002/wnan.1330

53. SoRelle ED, Liba O, Campbell JL, Dalal R, Zavaleta CL, de la Zerda A. A hyperspectral method to assay the microphysiological fates of nanomaterials in histological samples. *Elife.* 2016;5:e16352. doi:10.7554/eLife.16352

54. Al Faraj A, Shaik AP, Shaik AS. Effect of surface coating on the biocompatibility and in vivo MRI detection of iron oxide nanoparticles after intrapulmonary administration. *Nanotoxicology.* 2015;9(7):825–834. doi:10.3109/17435390.2014.980450